Biofilm 4 (2022) 100088

Contents lists available at ScienceDirect

Biofilm

journal homepage: www.sciencedirect.com/journal/biofilm

Quantifying biofilm propagation on chemically modified surfaces☆

Michelle C. Halsted [a], Amber N. Bible [b], Jennifer L. Morrell-Falvey [b], Scott T. Retterer [b,c,*]

[a] The Bredesen Center, University of Tennessee, Knoxville, TN, USA
[b] Biosciences Division, Oak Ridge National Laboratory, Oak Ridge, TN, USA
[c] Center for Nanophase Materials Sciences, Oak Ridge, TN, USA

ARTICLE INFO

Keywords:
Biofilm
Imaging
Honeycomb
Quantification
Quantitative
Image analysis
Surface

ABSTRACT

Conditions affecting biofilm formation differ among bacterial species and this presents a challenge to studying biofilms in the lab. This work leverages functionalized silanes to control surface chemistry in the study of early biofilm propagation, quantified with a semi-automated image processing algorithm. These methods support the study of *Pantoea* sp. YR343, a gram-negative bacterium isolated from the poplar rhizosphere. We found that *Pantoea* sp. YR343 does not readily attach to hydrophilic surfaces but will form biofilms with a "honeycomb" morphology on hydrophobic surfaces. Our image processing algorithm described here quantified the evolution of the honeycomb morphology over time, and found the propagation to display a logarithmic behavior. This methodology was repeated with a flagella-deficient *fliR* mutant of *Pantoea* sp. YR343 which resulted in reduced surface attachment. Quantifiable differences between *Pantoea* WT and Δ*fliR* biofilm morphologies were captured by the image processing algorithm, further demonstrating the insight gained from these methods.

1. Introduction

Biofilm formation and disruption have tremendous implications across a breadth of fields, including human health, agriculture, and chemical processing, [1–7]. Both physical and chemical cues mediate the processes by which these multicellular communities of bacteria attach and develop into complex architectures along natural and synthetic surfaces. Biofilm formation is often essential to the protection and propagation of microbial communities and can have significant consequences on the surrounding environment or host [8–11]. Developing strategies for selectively promoting or preventing biofilm formation requires a basic understanding of the factors that impact this process. Here we describe experimental methods that expand the current tools available for visualizing, analyzing, and quantifying biofilm formation. We demonstrate the utility of these methods by analyzing the biofilm formation of a microbial isolate from the poplar rhizosphere.

Physical and chemical factors collectively influence cell attachment and have a profound impact on biofilm propagation. Insight into these governing forces can be gained from fine control and manipulation of surface properties (e.g. hydrophobicity, surface roughness, surface topography) [12–20]. Bacteria can be cultured in nanofabricated and microfluidic platforms which offer exquisite control of surface properties through material deposition, topographic definition, and use of soft lithography. These platforms can also mitigate the challenges studying bacterial biofilms that are difficult to visualize and interrogate in their natural environments [19,21–28]. When paired with appropriate microscopy and image processing, these platforms can facilitate visualization and quantitative descriptions of bacterial growth and biofilm formation.

Self-assembled monolayers provide exquisite control of surface properties for biofilm studies via silane and thiol chemicals tuned with different chain-end functional groups [6,16,20,24,29–32]. The surface energy and reactivity can be readily modulated using commercially available reagents to modify silica, gold, and glass surfaces. One study utilized a hydrocarbon silane to survey attachment of *Staphylococcus epidermidis, Pseudomonas aeruginosa, Pseudomonas putida*, and *Escherichia coli* by performing cell counts from a video recording [6]. Friedlander et al. utilized thiol self-assembled monolayers to evaluate the role

* Corresponding author. Center for Nanophase Materials Sciences, Oak Ridge National Laboratory, Oak Ridge, TN, USA.
E-mail address: retterers t@ornl.gov (S.T. Retterer).

https://doi.org/10.1016/j.bioflm.2022.100088
Received 8 June 2022; Received in revised form 26 September 2022; Accepted 14 October 2022
Available online 15 October 2022

of hydrophobicity on flagella adhesion with quartz crystal microbalance and dissipation (QCM-D), which leverages the extreme resonance sensitivity of a quartz crystal to quantify absorbed mass by change in resonance frequency (2015). While this is a suitable approach to quantify overall cell attachment and revealed the importance of *E. coli* flagella in cell attachment to hydrophobic surfaces, these methods do not describe biofilm morphology [24]. Microscopy imaging combined with image processing can enumerate cell attachment and quantitatively describe morphology during the early stages of biofilm formation on functionalized substrates.

Imaging has been a hallmark of biological studies for centuries, providing qualitative descriptions of physical changes in biological systems since Hooke made the first observations of cells in the 17th century. Digital imaging has facilitated the evolution of qualitative description into more quantitative measurement and automated data extraction via image processing and analysis. Standard particle analysis functions can be applied to images of cells and bacterial colonies to perform high-throughput counts. Such features are available in image analysis programs such as cell-counter, OpenCFU, ColonyArea, NIST's Integrated Colony Enumerator (NICE), CellProfiler, and Biofilm Growth Intensity (BGI) algorithm [33–40]. The ready-to-use algorithms often demand little of the user in exchange for limited application [38,39]. As more image analysis tools have become readily available and more sophisticated, the extraction of quantitative information from microbial images to explain intuitive trends with quantitative data and increased statistical rigor has become more accessible [41–43]. Built-in particle analysis functions from ImageJ, MATLAB, or Python have been applied to images of microbial communities to describe surface coverage, shape, and connectivity of developing films [37,43]. Yang et al. demonstrated the ability of the Image Structure Analyzer software package to extract morphological characteristics of porosity and fractal dimension in monolayer biofilms (2001). In this work, a semi-automated ImageJ script was developed to quantify cell attachment and biofilm morphology from fluorescence microscopy images. When combined with automated image acquisition, these methods can extract numerical data from hundreds of images across multiple substrates in a relatively short period of time. This approach can be used to describe robust cell attachment dynamics of different bacterial species, as well as mixed microbial communities, across a variety of altered surface chemistries.

Our work examined the influence of hydrophobicity on *Pantoea* sp. YR343 attachment and biofilm propagation on silane-treated substrates in static conditions. *Pantoea* sp. YR343 was isolated from the rhizosphere of *Populus deltoides* and has been shown to promote plant growth [44]. *Pantoea* sp. YR343 was found to form biofilms with a honeycomb morphology on hydrophobic surfaces. ImageJ scripting was leveraged to quantitiatively describe this propagation pheonomenon. A flagella-defective mutant of *Pantoea* sp. YR343 was compared with the wild-type species using these methods to better understand the impact of flagella on *Pantoea* sp. YR343 biofilm propagation. Compared to the wildtype strain, the flagellar mutant showed delayed and reduced cell attachment as well as differences in biofilm morphology. Bacterial flagella are known to have a role in surface attachment and our results are consistent with consequences of limited motility and weak surface adhesion from a compromised flagellum [24].

2. Methods

2.1. Surface chemistry modification

Silicon wafers with silicon dioxide coating (Silicon Quest), were diced into 20 mm by 20 mm square chips. The chips were cleaned with pressurized air with a 0.2 μm filter, followed by a minimum of 5 min in a Harrick Plasma PDC-001 air plasma cleaner (Ithaca, NY). Vapor deposition was performed in an enclosed, glass dish on a hot plate with the following methods: 20 μL per 80 cm^2 trichloro(1H,1H,2H,2H-perfluorooctyl) silane (PFOTS) (Sigma-Aldrich, St. Louis, MO) for 4 h at 85 °C; 40 μL per 80 cm^2 3-aminopropyl trimethoxysilane (APTMS) (Gelest, Morrisville, PA) for 2 h at 150 °C; 40 μL per 80 cm^2 n-octadecyl (trimethoxy)silane (OTS) (Gelest, Morrisville, PA) for 2 h at 150 °C, followed by 2 h no heat; 4 h 65 °C Methoxytriethyleneoxypropyl-trimethoxysilane (MTMS) (Gelest, Morrisville, PA), followed by 1 h at 115 °C. Samples were characterized with a KRÜSS DSA 30 contact angle goniometer. 1 mL drop of distilled water was applied to the sample surface and contact angle measurements were made using the integrated software. Contact angle measurements were performed in triplicate.

2.2. Bacterial culture and device testing

Each experiment took place over the course of 3 days from the point of inoculation in liquid media to image collection. Engineered strains of *Pantoea* sp. YR343 expressing green fluorescent protein were engineered by expression of EGFP from a Gateway modified pBBR1-MCS5 plasmid, maintained with 10 μg ml^{-1} gentamycin [44]. *Pantoea* sp. YR343 were inoculated in R2A liquid medium (from a plate of R2A agar) and grown to stationary phase overnight. The next day, the overnight culture was diluted into fresh liquid media at a 1:100 dilution and the cells were grown to early exponential phase (approx. 4hrs) with a target optical density (OD) of 0.1, verified with a BioTek Synergy 2 microplate reader, 600 nm (measured with microtiter plate with 0.4 mL sample). Samples were diluted to 0.1 OD as needed.

The silane-treated substrates were each placed in concave dishes and filled with 3 mL of *Pantoea* sp. YR343 liquid culture, 0.1 OD (Fig. 1). Upon inoculation, the dishes were covered and incubated for a specified amount of time (i.e., the experimental time-point). Tweezers were used to gently remove the substrate from the liquid culture at a designated point in time, holding the sample at the corners to minimize impact on the biofilm. The substrate was rinsed with 10 mL DI water to remove loosely attached cells. Care was taken to apply each milliliter of DI water near the edge of the substrate and flow water across the sample. Pressurized air, blown through a 0.2 μL filter, was used to dry the sample. These experiments were conducted at a room temperature (around 60 °F).

2.3. Image collection

Image data was collected with an Olympus IX51 microscope (Shinjuku, Tokyo) complete with epifluorescence using a Chroma 41001FITC (Bellows Falls, VT) filter cube (480 nm excitation band pass filter with a 40 nm bandwidth and 535 nm emission band pass filter with a 50 nm bandwidth). A minimum of 10 images, from random positions across each 20 mm × 20 mm chip were acquired. Each experiment included multiple chips with 2–3 chips removed at each time point. Each experiment was performed at a minimum of two times with a minimum of 4 chips per time point and 10 acquired images per chip. *Pantoea* sp. YR343 WT attachment to PFOTS served as experimental controls in the flagella mutant experiments, and the time points from these experiments supplied additional experimental replicates to the Pantoea sp. YR343 WT dataset. Selected samples were imaged on an FEI Novalab 600 Dual-Beam System to collect Scanning Electron Microscopy (SEM) images of the *Pantoea* sp. YR343 cell attachment. Confocal fluorescence microscopy was performed using a Zeiss LSM710 confocal laser scanning microscope with a Plan-Apochromat 63x/1.40 oil immersion objective (Carl Zeiss Microimaging, Thornwood, NY).

2.4. Image processing

The open source software program ImageJ(Fiji) was used to analyze images. Image processing was carried out using a series of built-in functions run via automated scripts to convert fluorescence images into binary images and subsequently quantify 'gaps' in the bacterial biofilm via particle analysis. Individual adjustments in processing script parameters were made to ensure the binary images were representative

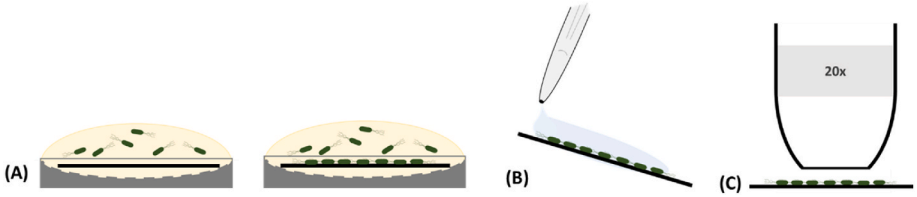

Fig. 1. Biofilm assay methods. A) Substrates were submerged in 3 mL of R2A growth media inoculated with *Pantoea* sp. YR343 at an optical density (OD_{600}) reading of 0.1, and incubated under static conditions to allow surface attachment and biofilm formation; B) Substrates were removed at selected times and rinsed with 10 mL of DI water and dried with pressurized air (0.2 μm filter); C) Imaging carried out using an Olympus IX51×, 20× objective.

of the original image of the bacterial biofilm. Scripts were tailored for each stack of images to account for differences in microscope settings and fluorescence intensity that changed over the course of the experimental study. ImageJ scripts used a combination of background subtraction, thresholding, and particle analysis functions. Threshold functions, commonly found across image processing platforms, identify foreground objects based on differences in pixel intensity with that of background objects. Pixels are then reassigned as white (background) or black (objects) to create a binary image [45]: [46]. A particle analysis function, also common across image processing platforms, can then identify objects (i.e. black pixels) present in the binary image [36,37,43]. Sample ".ijm" scripts are provided in the supplementary materials (S.6 and S.7). *Pantoea* sp. YR343 is 1–3 μm in length, approximately 0.5–15 μm in width which corresponds to approximately 4.5 μm^2 (3 x 1.5) or roughly 18 pixels (~4.7 μm^2). The gap analysis limit was set to 18 pixels such that the analyses focuses on the morphology of features greater than that of a single cell. The gaps in the honeycomb biofilm morphology were the objects identified by the ImageJ(Fiji) particle analysis function. Metrics on the number of gaps, individual gap size, and total percentage of gap area coverage in the biofilm were recorded. The difference between the total area of the image minus the total gap area is reported as the surface area coverage of the biofilm. For reference, the total image is 1,376,256 pixels (1344 pixels X 1024 pixels) with a 20x objective having a calibration of ~0.51 μm/pixel length or 0.26 μm^2/pixel area. A subregion of 710 pixels X 564 pixels within each image was used for analysis to accommodate for nonuniform illumination across the microscope field of view. Fig. 2 outlines the image processing steps with illustrations. The scripts are provided in the supplemental materials (S.6 and S.7) and includes comments to guide users in adjusting parameters.

2.5. Mutant strain construction

The Δ*fliR* mutant was generated as described previously [44]. Briefly, a 1000 base pair sequence both upstream and downstream of the *fliR* gene was amplified and cloned into pK18mobsacB, then introduced into *Pantoea* sp. YR343 via electroporation. Colonies were selected based on resistance to kanamycin at 50 μg ml-1 and then grown in rich media for at least three passages to allow the cells to undergo homologous recombination and lose the plasmid. Mutant candidates were then screened for a loss of motility and confirmed using PCR.

3. Results & discussion

Pantoea sp. YR343 is a rod-shaped, flagellated, gram-negative bacterium isolated from the Poplar rhizosphere and has been shown to exhibit biofilm formation, swimming motility, and surface motility [44]. *Pantoea* sp. YR343 has been engineered to express green fluorescent protein (GFP), facilitating the use of fluorescence microscopy for quantifying cell attachment and surface coverage. Alternatively, live dead/staining or bright field imaging could be utilized within this workflow to image non-fluorescent species. Silane chemistry was leveraged to examine the impact of surface energy on cell attachment. Silicon dioxide coated substrates (e.g., silicon, glass) were modified with the following terminal surface chemistries: a fluorinated chain, a hydrocarbon chain, an ester, and an amine group. These substrates were characterized by their water contact angle, as indicated in Table 1.

Pantoea sp. YR343 attachment to the functionalized substrates was tested under static conditions, appropriate replicates and controls were performed. Substrates were submerged in 3 mL of R2A culture medium inoculated with *Pantoea* sp. YR343-GFP, at an optical density of 0.1 (at 600 nm). Substrates were removed from the culture at specified time points and rinsed with 10 mL distilled water to remove loosely attached cells. The substrate was dried with pressurized air to minimize drying artifacts and subsequently imaged with a fluorescence microscope (Fig. 1). Fluorescence images of the bacterial biofilm propagation were collected from multiple positions across each sample to capture representative cell behavior. Image processing and analysis of cell area coverage and biofilm morphology was performed using ImageJ(FIJI) scripts.

The effect of hydrophobicity on *Pantoea* sp. YR343 cell attachment is summarized in Fig. 3. After 20 h, *Pantoea* sp. YR343 biofilm surpassed 70% area coverage on the hydrophobic surfaces (PFOTS and OTS), with neglible attachment to the hydrophilic surfaces (APTMS and MTMS). Differences of mean values of surface coverage for all conditions were statistically different from one another based on a *t*-test comparsion between conditions. There was no visible attachment to the control surfaces of glass, silicon, and quartz (data not shown). These results are consistent with the literature as many bacterial species have been shown to be negatively charged and favor attachment to hydrophobic, neutral

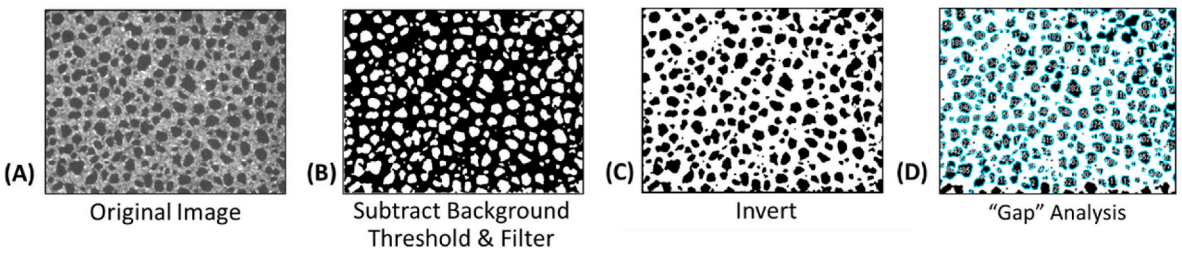

Fig. 2. Image processing and quantification of honeycomb biofilm pattern. Cells are grey in the original image (A) and black in the binary image (B). The image is inverted (C), and the particle analysis function is applied to gaps (black) in the image (D). Each image shown is a 710 pixel x 564 pixel (~360 μm × 286 μm area) subregion representative of those used for analysis.

Table 1
Summary of silane acronyms and water contact angle measurements, ±0.1 Std Dev.

	PFOTS	OTS	MTMS	APTMS
Chemical Name	Trichloro (1H, 1H, 2H, 2H-perfluoroctyl) silane	n-octadecyl (trimethoxy) silane	Methoxytriethyleneoxypropyl- trimethoxy silane	3-aminopropyl trimethoxy silane
Surface Property	Hydrophobic	Hydrophobic	Hydrophilic	Hydrophilic
Water Contact Angle	104.4°	92.5°	45.2°	53.4°

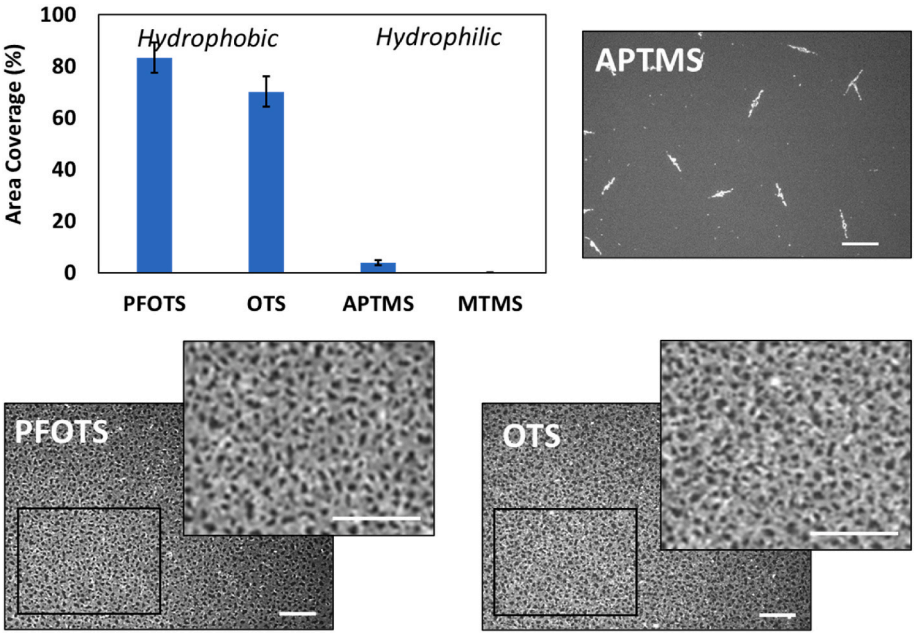

Fig. 3. *Pantoea* sp. YR343 area coverage on hydrophobic and hydrophilic surfaces after 20 h: *Pantoea* sp. YR343 attachment to Trichloro(1H,1H,2H,2H-perfluorooctyl) silane (PFOTS, 104.4° contact angle), n-octadecyl (trimethoxy) silane (OTS, 92.5° contact angle), 3-aminopropyl trimethoxy silane (APTMS, 53.4° contact angle), and Methoxytriethyleneoxypropyl-trimethoxy silane (MTMS, 45.2° contact angle). Error bars represent standard deviation in cell area coverage (%) from a minimum dataset of 30 images, acquired from 3 replicate treatments. Scale bar 25 μm.

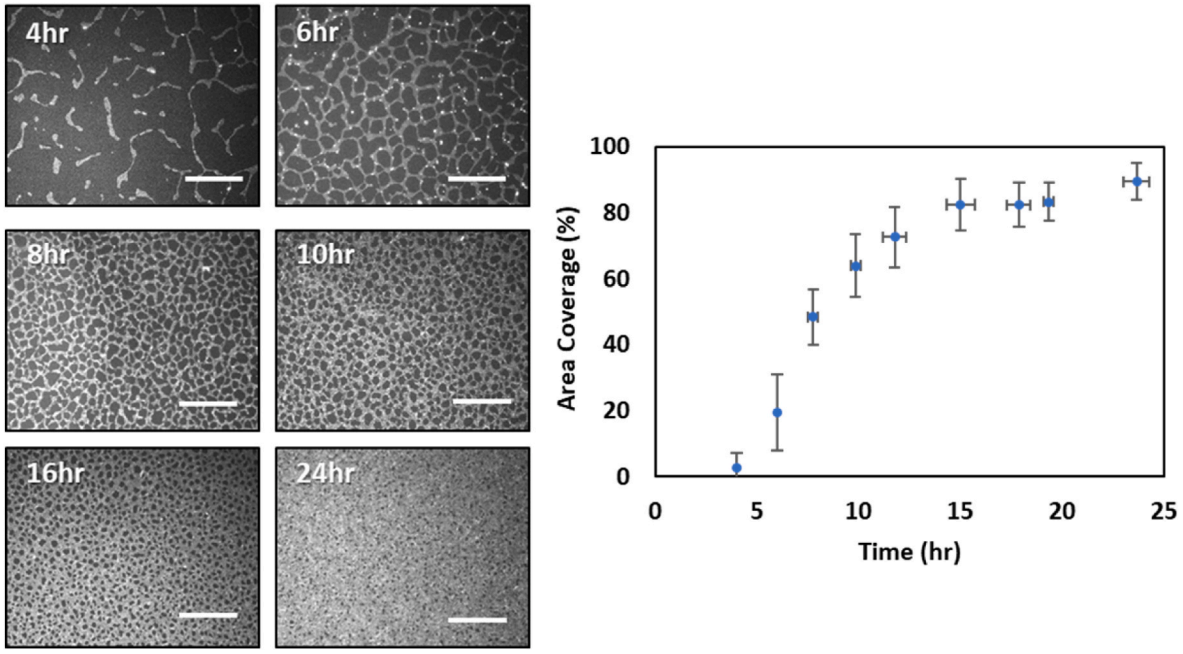

Fig. 4. *Pantoea* sp. YR343 attachment to Trichloro(1H,1H,2H,2H-perfluorooctyl) silane (PFOTS), average area coverage for each time point. Error bars represent standard deviation in cell area coverage (%) on the y-axis and standard deviation in sampling time point on the x-axis; a minimum dataset of 30 images collected from replicates of each time point and experimental replicates with a total dataset of 576 images. Image scale bar 50 μm.

surfaces [1,11,47,48].

3.1. Propagation of honeycomb biofilm morphology

Honeycomb biofilm morophology (also referred to as web-like, net-like, networks, and branching morphology) is not unique to *Pantoea* sp. YR343, and has been previously observed in the literature under a variety of conditions (e.g. static conditions, fluid flow; stainless steel coupon, polystyrene microtiter plate; mixed biofilm, pure culture; wet biofilm, dried biofilm), with both Gram-negative and Gram-positive bacterial strains [1,49–55]. In this work, ImageJ(Fiji) scripts were used to quantify the evolution of *Pantoea* sp. YR343 biofilm morphology based on the number and size of gaps observed in the honeycomb pattern. Fig. 4 depicts *Pantoea* sp. YR343 attachment to PFOTS with an average area coverage for each time point, with representative images to illustrate the evolution of the honeycomb biofilm morphology.

As shown in Fig. 4, the *Pantoea* sp. YR343 biofilm begins with linear branches of cells, which extend in length, and intersect with other branches to create a net-like or honeycomb appearance. The honeycomb gaps are segmented with branches of cells as the biofilm continues to

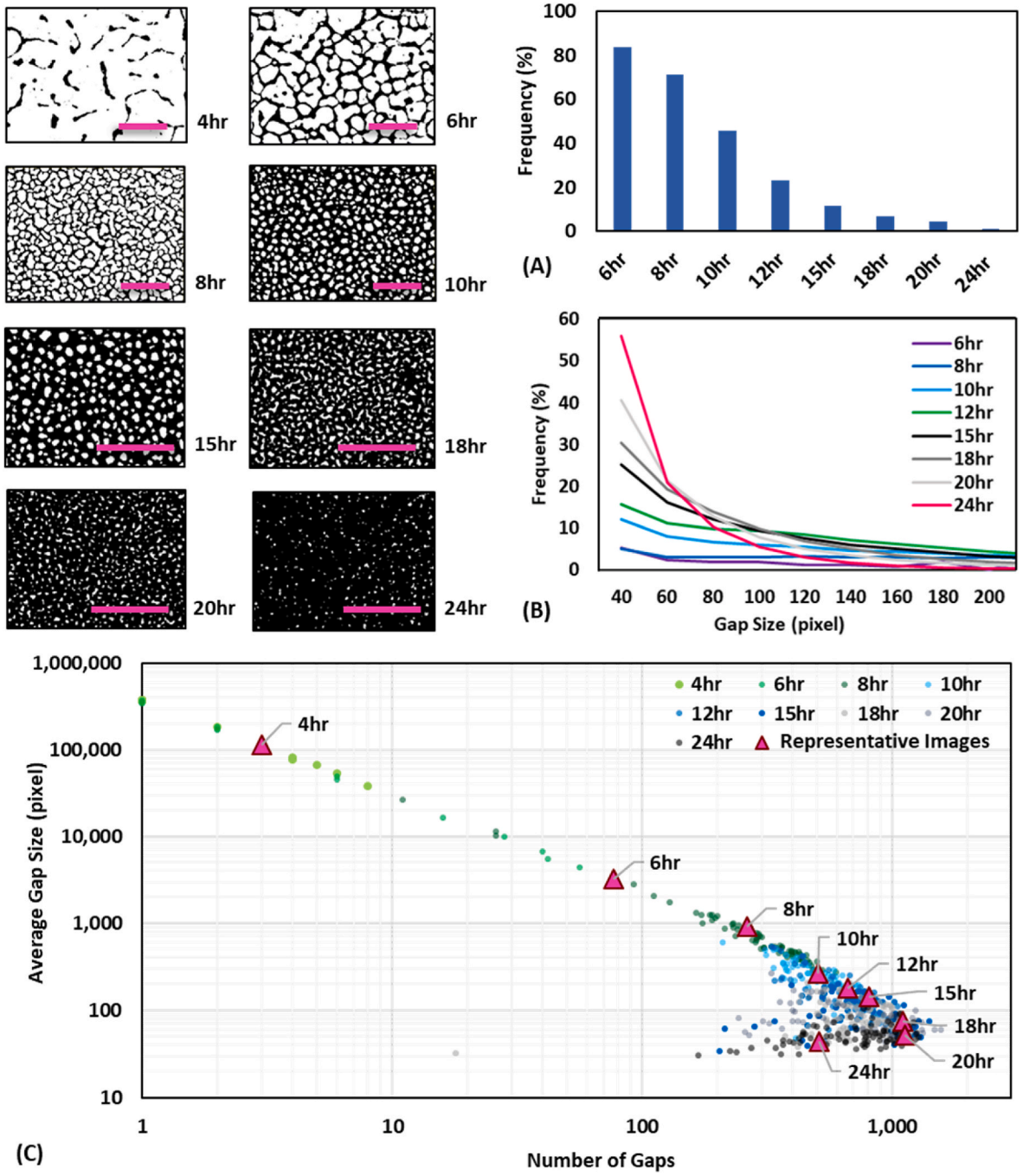

Fig. 5. Characterization of *Pantoea* sp. YR343 morphology with gap size and number. A) Percentage of gap sizes greater than 200 pixels (~52 μm^2) for each time point. Representative images of each timepoint are shown on the left, scale bar is 50 μm. B) Distribution of gap size across *Pantoea* sp. YR343 dataset (percentage of gaps exceeding 200 pixels (~52 μm^2) size is not shown in plot). C) Relationship between average gap size and number per image, represented by a data point, constructed from 576 images; pink triangle data points on the plot correspond to the representative images on the left. (For interpretation of the references to colour in this figure legend, the reader is referred to the Web version of this article.)

propagate. This consequently decreases the gap size and increases the number of gaps in the honeycomb biofilm. The gaps become smaller and many of the gaps are eventually filled by cells. Substantially fewer gaps remain in the 24-h dataset. Gaps less than the cell size may be present but have been excluded from these analyses due to the minimum allowable gap sizes. These visual observations are supported with quantitative information extracted from the image via gap analysis (Fig. 5).

Fig. 5, A shows the frequency of gaps greater than 200 pixels (~52 μm^2 area) for at each time point. Fig. 5, B shows the gap size distribution at each time point, based on a range of 18–200 pixels (4.5 μm^2–52 μm^2). The 4-h dataset is not included in the analyses because the morphology is dominated by unconnected, linear branches of cells at this time point. The few gaps that formed during the 4-h time point are on the order of 10,000 and 100,000 pixels.

The percentage of *Pantoea* sp. YR343 gaps incrementally decrease as the gap size bin increases, and this is consistent with the logarithmic relationship between the average gap size for an image, and the number of gaps, which decreased as time progressed (Fig. 5, C). Fig. 5, B shows that approximately 40% of the 20-h dataset is comprised of gaps with less than 40 pixels (~10 μm^2) in size, and this jumps to 60% in the 24-h dataset. The increasing percentage of 40-pixel (~10 μm^2) and 60-pixel (~16 μm^2) gap sizes in Fig. 5, B indicates cells are filling the gaps as time progresses, and this is consistent with cells covering 90% of the surface area after 24 h (Fig. 4).

Fig. 5, C illustrates an exponential decrease in average gap size, joined by an exponential increase in the number of gaps. From this logarithmic behavior, we infer *Pantoea* sp. YR343 cells segment gaps in the honeycomb biofilm as part of the biofilm propagation mechanism where one large gap becomes two small gaps, and the average size of these two gaps equates to half the size of the large gap. This behavior follows a slope of −1, which is the approximate slope of the *Pantoea* sp. YR343 dataset in Fig. 5, C between 4 and 15 h. Many, but not all, of the gaps in the honeycomb biofilm eventually become so small that they are filled by cells (18–24 h), and this consequently decreases the number of gaps (i.e. creates a bend in the dataset). The representative images show in Fig. 5, C correspond to the triangle data points and offer a simplified example. Supplementary Materials Figure S1 offers a complementary plot relating average gap size for each dataset with respect to time.

The images shown in Fig. 5 are a monolayer of the *Pantoea* sp. YR343 biofilm, confirmed by Scanning Electron Microscopy (Supplementary Materials, Figure S2). It is highly plausible the rinse step removed loosely attached cells from a multi-dimensional biofilm matrix. In a three-dimensional biofilm, honeycomb gaps would result in a porous biofilm, facilitating mass transfer of nutrients, waste, and oxygen [1,4,56,55].

3.1.1. Propagation of flagella mutant biofilms

Flagella play a key role in the initial stages of biofilm formation. In addition to providing a motor for swimming and surface motility, flagella can mediate attachment by overcoming repulsive forces near the surface [4,11,24,57–59]. Flagella increase the surface area of attachment and have been shown to anchor cells to surfaces [11,20,24,57]. Like *Pantoea* sp. YR343, *Listeria monocytogenes* form honeycomb biofilms and flagella have been demonstrated to play an integral role in this morphology as the absence of flagella resulted in unstructured biofilms; note that while *Listeria monocytogenes* is known for its pathogenic behavior, *Pantoea* sp. YR343 studies have found no evidence of pathogenic behavior to date [53]. To test whether our method could distinguish different biofilm morphologies, we examined biofilm formation using a *Pantoea* sp. YR343 mutant defective in flagella assembly due to deletion of the gene encoding FliR (Fig. 6).

FliR is a conserved integral membrane protein in the basal body complex that plays a key role in the structure and function of the flagellar export apparatus [60]. Using this mutant, we found that the area coverage of Δ*fliR* biofilms is approximately half that of wildtype biofilms, yet the standard deviation is approximately doubled (Fig. 6). Mean surface coverage for the WT and mutant strains were significantly different based on *t*-test comparison. When examined with SEM, no flagella were observed on the mutant cells (Supplementary Materials, Figure S3, S4). The variation may be explained by the decrease in surface adhesion due to loss of the flagella adhesin. Consistent with previous reports, a lack of flagella or defects to the flagella adhesin likely explains the Δ*fliR* area coverage and variation [19,24,52,57]. Relatively large sections of the biofilm appeared to detach during the rinse step, and these experimental observations align with the notion that the Δ*fliR* biofilm lacks sufficient adhesion.

Pantoea sp. YR343 Δ*fliR* biofilm morphology was quantified and compared to wild type cells (Fig. 7). This analysis shows that there are dramatic differences in the gap size distribution, many of the gaps in the *Pantoea* sp. YR343 Δ*fliR* dataset exceed 200 pixels (Figure S5, A). Interestingly, gap sizes below 200 pixels in the Δ*fliR* dataset are evenly distributed across time points (Figure S5, B). This is consistent with Fig. 7, A which shows a scattered relationship between average gap size and number that does not change with respect to time. In other words, the *Pantoea* sp. YR343 Δ*fliR* dataset may follow the same spatial trend as *Pantoea* sp. YR343 WT but does not follow the temporal trend (Fig. 7, A), progressing more slowly and with weaker attachment.

Fig. 7, B captures the differences in the *Pantoea* sp. YR343 Δ*fliR* and WT morphology by comparing metrics of two (representative) biofilm images with equal surface area coverage. The radius of the bubble corresponds to the standard deviation in the image gap size, and the dot in the center of the bubble indicates the average gap size for each image. The radius of the bubble is independent of the gap number and is represented by bubble position.

Silane chemical modifications and image processing can be applied to all sorts of bacterial biofilm studies, together and separately. Silane chemical modifications can be applied to glass substrates to allow for brightfield microscopy or confocal microscopy. The image processing framework is also compatible with brightfield images, provided there is minimal background noise. The challenge, particularly with a time-lapse experimental set-up, is distinguishing cells that have actively attached to the substrate from cells in the image background. The image processing framework can be applied to other surfaces provided that a threshold

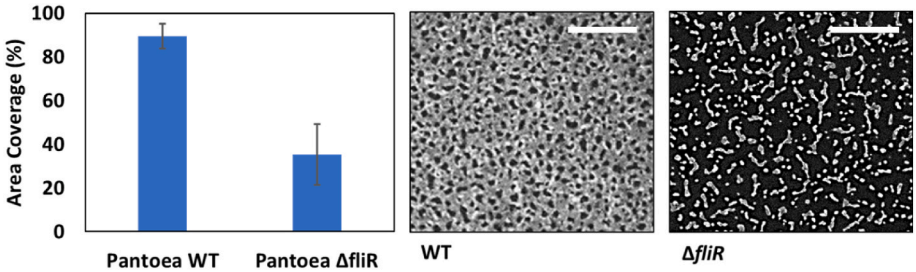

Fig. 6. Effect of *Pantoea* sp. YR343 flagella on attachment to PFOTS at 24-h time point, scale bar 25 μm. Error bars represent standard deviation in cell area coverage from a minimum dataset of 30 images, acquired from a minimum of 3 replicate treatments.

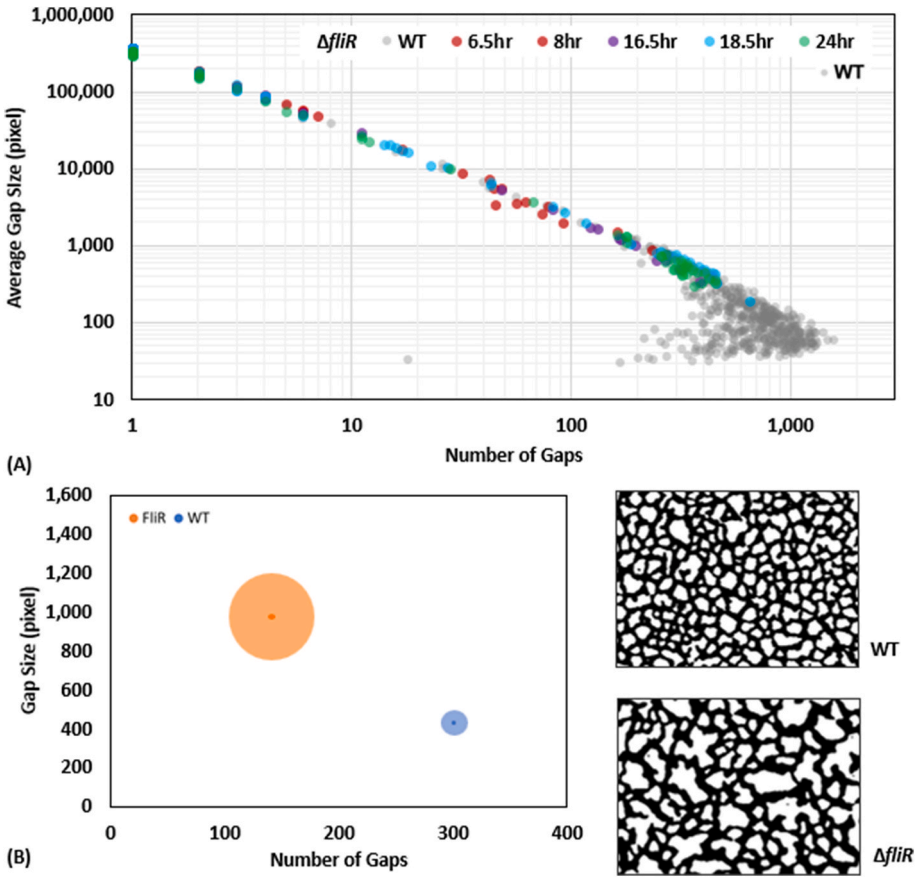

Fig. 7. Differences between *Pantoea* sp. YR343 WT and *Pantoea* sp. YR343 Δ*fliR* biofilm morphology on PFOTS surface. A) Relationship between Δ*fliR* average gap size and number per image, represented by each data point and overlaid on WT dataset. B) Quantitative comparison of biofilm morphology where bubble size denotes standard deviation in gap size, with representative images for *Pantoea* sp. YR343 WT (53% area coverage) and *Pantoea* sp. YR343 Δ*fliR* (52% area coverage).

function can distinguish bacteria attachment from the background and imaging artifacts. Fluorescence microscopy offers the advantage of imaging opaque surfaces with the image processing framework.

Silane chemical modifications is compatible with confocal microscopy experimental set-up and offers the advantage of capturing three-dimensional data of the bacterial biofilm in liquid culture. These methods, along with scanning electron microscopy, are depicted in Fig. 8. Fig. 8 also includes time-lapse images of the *Pantoea* sp. YR343 biofilm propagation captured with the confocal microscope; this experimental method observes cell attachment to the same substrate with liquid culture and does not include a rinse step. The honeycomb biofilm is visible in each of these microscopy images, and the three-dimensional profile of the biofilm appears to have a dense layer of cells at 24 h. We believe this profile consists of loosely attached cells, possibly accrued from settling artifacts, and these cells washed away during the rinse step at the end of the experimental time-lapse. During these experiments it became clear that temperature affects the rate of biofilm propagation, and future work will include temperature and the three-dimensional biofilm studies.

Electron microscopy offers the advantage of examining bacterial biofilms on sub-micron scales (Fig. 8). Scanning electron microscopy images of the *Pantoea* sp. YR343 biofilm revealed a monolayer biofilm with flagella spanning the honeycomb gaps (Fig. 8, G). The flagella often appeared to be intertwined, and occasionally chains of cells extended from one side of the biofilm, into the gap, alongside the flagella. This suggests the cells were segmenting the honeycomb gap when the experiment ended. Conceivably, the flagella may guide nascent cells to segment the gap by providing additional points of attachment to the biofilm (Fig. 8, G). These observations prompted experiments with the flagella defective mutant to understand the role of flagella in *Pantoea* sp. YR343 biofilm propagation. There were no visible flagella in SEM images of *Pantoea* sp. YR343 Δ*fliR* (Supplementary Materials, Figure S3, S4). Flagella offer adhesion benefits to early biofilm propagation; the observed flagella absence may explain the differences in area coverage and not just compromised motility. Additionally, the flagella may serve as an attachment site for motile cells to anchor to. This is consistent with observations from live biofilm imaging with the confocal microscope where cells were observed to be spinning on an axis, like a ball joint, as though the cells were tethered. Fig. 8 demonstrates the complementary advantages across microscopy methods, and together these methods revealed a unique mechanism for biofilm propagation.

4. Conclusions

Our methods leverage the ease of fluorescence microscopy to generate large datasets, across multiple surfaces and samples, necessary for capturing the natural variation and distribution of biological phenomenon. This approach will complement the qualitative data gathered from confocal and scanning electron microscopy, which are resource intensive and time consuming. We demonstrated how this alternative biofilm assay quantifies cell attachment and early biofilm formation on silane-treated surfaces. The semi-automated image processing script captures numerical data from biofilm morphology and unveiled considerable differences between the morphology of *Pantoea* sp. YR343 WT and *Pantoea* sp. YR343 Δ*fliR* biofilms. Future work aims to explore mixed communities of poplar microbial isolates using this platform together with bacterial species expressing various fluorescent proteins.

Additionally, our approach quantifies spatial temporal data

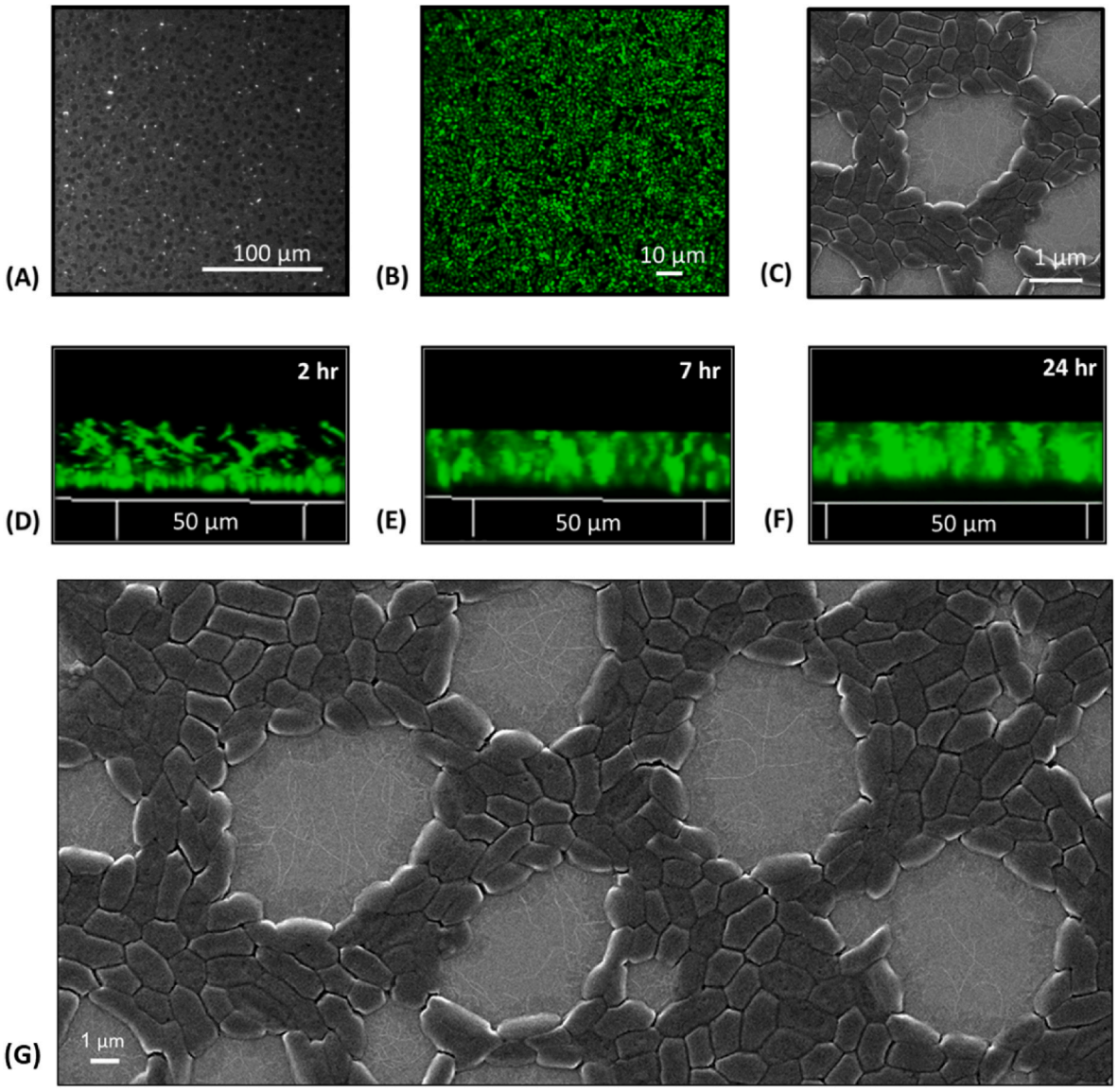

Fig. 8. An evaluation of *Pantoea* sp. YR343 biofilm propagation on PFOTS-silicon substrate using different microscopy methods. A) Fluorescence microscopy after 10 h attachment. Sample was rinsed with 10 mL DI water and dried with pressurized air. B) Scanning Electron Microscopy after 10 h of attachment. Sample was rinsed with 10 mL DI water, dried with pressurized air, and coated with 5 nm gold. C) Wet biofilm at 13 h, Confocal Laser Scanning Microscopy. D) Vertical profile of *Pantoea* sp. YR343 biofilm at 2 h. E) Vertical profile of *Pantoea* sp. YR343 biofilm at 7 h. F) Vertical profile of *Pantoea* sp. YR343 biofilm at 24 h. G) *Pantoea* sp. YR343 biofilm propagation on PFOTS-Si substrate, 24 h (Zeiss Scanning Electron Microscope, 5 nm gold coating). (For interpretation of the references to colour in this figure legend, the reader is referred to the Web version of this article.)

qualitatively observed in microscopy images of biofilm propagation. This numerical data enables data analysis like statistics, regression analysis, theoretical equations, and numerical metrics for computer simulations. Collectively, novel and traditional methods will be essential in unraveling the complexities of biofilm formation.

Author credit statement

Michelle C. Halsted - Conceptualization; Data curation; Formal analysis; Investigation; Methodology, Visualization, Writing – original draft; Writing – review & editing. Amber N. Bible – Experimentation, Resources, Methodology; Writing – review & editing. Jennifer L. Morrell-Falvey – Conceptualization, Resources, Writing – review & editing. Scott T. Retterer – Conceptualization, Data curation, Formal analysis, Funding acquisition, Investigation, Methodology, Project administration, Resources, Supervision, Roles/Writing – original draft, Writing – review & editing.

Declaration of competing interest

The authors declare the following financial interests/personal relationships which may be considered as potential competing interests: Scott T. Retterer reports financial support was provided by US Department of Energy. Michelle Halsted reports was provided by US Department of Energy. Jennifer Morrell-Falvey reports financial support was provided by US Department of Energy. Amber Bible reports financial support was provided by US Department of Energy.

Data availability

Data will be made available on request.

Acknowledgements

This work was supported by the Office of Science, Biological and

Environmental Research, as part of the Plant Microbe Interfaces Scientific Focus Area (http://pmi.ornl.gov). Scanning electron microscopy was carried out at the Center for Nanophase Materials Sciences, which is a DOE Office of Science User Facility.

Appendix A. Supplementary data

Supplementary data to this article can be found online at https://doi.org/10.1016/j.bioflm.2022.100088.

References

[1] Donlan RM. Biofilms: microbial life on surfaces. Emerg Infect Dis 2002;8(9):881–90. https://doi.org/10.3201/eid0809.020063.

[2] Bendaoud M, Vinogradov E, Balashova NV, Kadouri DE, Kachlany SC, Kaplan JB. Broad-spectrum biofilm inhibition by Kingella kingae exopolysaccharide. J Bacteriol 2011;193(15):3879. https://doi.org/10.1128/JB.00311-11.

[3] Schultz D, Onuchic JN, Ben-Jacob E. Turning death into creative force during biofilm engineering. Proc Natl Acad Sci USA 2012;109(46):18633–4. https://doi.org/10.1073/pnas.1215227109.

[4] Petrova OE, Sauer K. Sticky situations: key components that control bacterial surface attachment. J Bacteriol 2012;194(10):2413–25. https://doi.org/10.1128/jb.00003-12.

[5] Kim J, Park HD, Chung S. Microfluidic approaches to bacterial biofilm formation. Molecules 2012;17(8):9818–34. https://doi.org/10.3390/molecules17089818.

[6] Wang H, Sodagari M, Ju L-K, Zhang Newby B-m. Effects of shear on initial bacterial attachment in slow flowing systems. Colloids Surf B Biointerfaces 2013;109:32–9. https://doi.org/10.1016/j.colsurfb.2013.03.016.

[7] Fish K, Osborn AM, Boxall JB. Biofilm structures (EPS and bacterial communities) in drinking water distribution systems are conditioned by hydraulics and influence discolouration. Sci Total Environ 2017;593–594:571–80. https://doi.org/10.1016/j.scitotenv.2017.03.176.

[8] Sutherland IW. Biofilm exopolysaccharides: a strong and sticky framework. Microbiology 2001;147(1):3–9. https://doi.org/10.1099/00221287-147-1-3.

[9] Little AEF, Robinson CJ, Peterson SB, Raffa KE, Handelsman J. Rules of engagement: interspecies interactions that regulate microbial communities annual review of microbiology, vol. 62; 2008. p. 375–401.

[10] Hochbaum AI, Aizenberg J. Bacteria pattern spontaneously on periodic nanostructure arrays. Nano Lett. 2010;10(9):3717–21. https://doi.org/10.1021/nl102290k.

[11] Berne C, Ellison CK, Ducret A, Brun YV. Bacterial adhesion at the single-cell level. Nat Rev Microbiol 2018;16(10):616–27. https://doi.org/10.1038/s41579-018-0057-5.

[12] Mozes N, Marchal F, Hermesse MP, Van Haecht JL, Reuliaux L, Leonard AJ, Rouxhet PG. Immobilization of microorganisms by adhesion: interplay of electrostatic and nonelectrostatic interactions. Biotechnol Bioeng 1987;30(3):439–50. https://doi.org/10.1002/bit.260300315.

[13] Costerton JW, Stewart PS, Greenberg EP. Bacterial biofilms: a common cause of persistent infections. Science 1999;284(5418):1318–22. https://doi.org/10.1126/science.284.5418.1318.

[14] Gottenbos B, van der Mei HC, Klatter F, Nieuwenhuis P, Busscher HJ. In vitro and in vivo antimicrobial activity of covalently coupled quaternary ammonium silane coatings on silicone rubber. Biomaterials 2002;23(6):1417–23. https://doi.org/10.1016/S0142-9612(01)00263-0.

[15] Garrett TR, Bhakoo M, Zhang Z. Bacterial adhesion and biofilms on surfaces. Prog Nat Sci 2008;18(9):1049–56. https://doi.org/10.1016/j.pnsc.2008.04.001.

[16] Glass NR, Tjeung R, Chan P, Yeo LY, Friend JR. Organosilane deposition for microfluidic applications. Biomicrofluidics 2011;5(3):36501–365017. https://doi.org/10.1063/1.3625605.

[17] Epstein AK, Hochbaum AI, Kim P, Aizenberg J. Control of bacterial biofilm growth on surfaces by nanostructural mechanics and geometry. Nanotechnology 2011;22(49):494007. https://doi.org/10.1088/0957-4484/22/49/494007.

[18] Harimawan A, Rajasekar A, Ting Y-P. Bacteria attachment to surfaces – AFM force spectroscopy and physicochemical analyses. J Colloid Interface Sci 2011;364(1):213–8. https://doi.org/10.1016/j.jcis.2011.08.021.

[19] Friedlander RS, Vlamakis H, Kim P, Khan M, Kolter R, Aizenberg J. Bacterial flagella explore microscale hummocks and hollows to increase adhesion. Proc Natl Acad Sci USA 2013;110(14):5624–9. https://doi.org/10.1073/pnas.1219662110.

[20] Tuson HH, Weibel DB. Bacteria–surface interactions. Soft Matter 2013;9(17):4368–80. https://doi.org/10.1039/C3SM27705D.

[21] Timm CM, Hansen RR, Doktycz MJ, Retterer ST, Pelletier DA. Microstencils to generate defined, multi-species patterns of bacteria. Biomicrofluidics 2015;9(6):064103. https://doi.org/10.1063/1.4935938.

[22] Timm AC, Halsted MC, Wilmoth JL, Retterer ST. Assembly and tracking of microbial community development within a microwell Array platform. JoVE 2017;124. https://doi.org/10.3791/55701.

[23] Hol FJH, Dekker C. Zooming in to see the bigger picture: microfluidic and nanofabrication tools to study bacteria. Science 2014;346(6208):1251821. https://doi.org/10.1126/science.1251821.

[24] Friedlander RS, Vogel N, Aizenberg J. Role of flagella in adhesion of Escherichia coli to abiotic surfaces. Langmuir 2015;31(22):6137–44. https://doi.org/10.1021/acs.langmuir.5b00815.

[25] Halsted M, Wilmoth JL, Briggs PA, Hansen RR, Briggs DP, Timm AC, Retterer ST. Development of transparent microwell arrays for optical monitoring and dissection of microbial communities. J Vac Sci Technol B 2016;34(6):06KI03. https://doi.org/10.1116/1.4962739.

[26] Shankles PG. Interfacing to biological systems using microfluidics. PhD dissertation, University of Tennessee; 2018. https://trace.tennessee.edu/utk_graddiss/5315.

[27] Aufrecht J. In: Custom-engineered micro-habitats for characterizing rhizosphere interactions". PhD dissertation. University of Tennessee; 2019. https://trace.tennessee.edu/utk_graddiss/5454.

[28] Halsted MC. Approaches to studying bacterial biofilms in the bioeconomy with nanofabrication techniques and engineered platforms. PhD dissertation, University of Tennessee; 2020. https://trace.tennessee.edu/utk_graddiss/6075.

[29] Tan CP, Craighead HG. Surface engineering and patterning using parylene for biological applications. Materials 2010;3(3):1803–32. https://doi.org/10.3390/ma3031803.

[30] Privett BJ, Youn J, Hong SA, Lee J, Han J, Shin JH, Schoenfisch MH. Antibacterial fluorinated silica colloid superhydrophobic surfaces. Langmuir 2011;27(15):9597–601. https://doi.org/10.1021/la201801e.

[31] Maroni P, Montes Ruiz-Cabello FJ, Cardoso C, Tiraferri A. Adsorbed mass of polymers on self-assembled monolayers: effect of surface chemistry and polymer charge. Langmuir 2015;31(22):6045–54. https://doi.org/10.1021/acs.langmuir.5b01103.

[32] Galbiati M. Introduction to self-assembled monolayers. 2016. p. 45–81.

[33] Heydorn A, Nielsen AT, Hentzer M, Sternberg C, Givskov M, Ersbøll BK, Molin S. Quantification of biofilm structures by the novel computer program comstat. Microbiology 2000;146(10):2395–407. https://doi.org/10.1099/00221287-146-10-2395.

[34] Sieuwerts S, De Bok FAM, Mols E, De Vos WM, Van Hylckama Vlieg JET. A simple and fast method for determining colony forming units. Appl Microbiol 2008;47(4):275–8. https://doi.org/10.1111/j.1472-765X.2008.02417.x.

[35] Carpenter AE, Jones TR, Lamprecht MR, et al. CellProfiler: image analysis software for identifying and quantifying cell phenotypes. Genome Biol 2006;7:R100. https://doi.org/10.1186/gb-2006-7-10-r100.

[36] Clarke, M. L., Burton, R. L., A.Hill, N., Litorja, M., Nahm, M. H., and Hwang, J. Low-cost, high-throughput, automated counting of bacterial colonies. Cytometry. 77A(8), 790-797. doi.org/10.1002/cyto.a.20864.

[37] Cai W-J, Hu X, Huang W-J, Murrell MC, Lehrter JC, Lohrenz SE, Gong G-C. Acidification of subsurface coastal waters enhanced by eutrophication. Nat Geosci 2011;4(11):766–70. https://doi.org/10.1038/ngeo1297.

[38] Guzmán C, Bagga M, Kaur A, Westermarck J, Abankwa D. PLOS ONE. ColonyArea: an ImageJ plugin to automatically quantify Colony formation in clonogenic assays. 2014. https://doi.org/10.1371/journal.pone.0092444.

[39] Larimer C, Winder E, Jeters R, et al. A method for rapid quantitative assessment of biofilms with biomolecular staining and image analysis. Anal Bioanal Chem 2016;408:999–1008. https://doi.org/10.1007/s00216-015-9195-z.

[40] Geissmann Q. OpenCFU, a new free and open-source software to count cell colonies and other circular objects. PLoS One 2013;8(2):e54072. https://doi.org/10.1371/journal.pone.0054072.

[41] Yang X, Beyenal H, Harkin G, Lewandowski Z. Evaluation of biofilm image thresholding methods. Water Res 2001;35(5):1149–58. https://doi.org/10.1016/s0043-1354(00)00361-4.

[42] Verma OP, Sharma R, Kumar D. Binarization based image edge detection using bacterial foraging algorithm. Proc. Technol. 2012;6:315–23. https://doi.org/10.1016/j.protcy.2012.10.038.

[43] Choudhry P. High-throughput method for automated colony and cell counting by digital image analysis based on edge detection. PLoS One 2016;11(2):e0148469. https://doi.org/10.1371/journal.pone.0148469.

[44] Bible AN, Fletcher SJ, Pelletier DA, Schadt CW, Jawdy SS, Weston DJ, Morrell-Falvey JL. A carotenoid-deficient mutant in *Pantoea* sp. YR343, a bacteria isolated from the rhizosphere of Populus deltoides, is defective in root colonization. Front Microbiol 2016;7(491). https://doi.org/10.3389/fmicb.2016.00491.

[45] Ljosa V, Carpenter A. Introduction to the quantitative analysis of two-dimensional fluorescence microscopy images for cell-based screening. PLoS Comput Biol 2009;5(12):e1000603. https://doi.org/10.1371/journal.pcbi.1000603.

[46] Cardullo RA. Fundamentals of image processing in light microscopy. Methods Cell Biol 2003;72:217–42. https://doi.org/10.1016/S0091-679X(03)72011-1.

[47] Mai TL, Conner DE. Effect of temperature and growth media on the attachment of Listeria monocytogenes to stainless steel. Int J Food Microbiol 2007;120(3):282–6. https://doi.org/10.1016/j.ijfoodmicro.2007.09.006.

[48] Song F, Koo H, Ren D. Effects of material properties on bacterial adhesion and biofilm formation. J Dent Res 2015;94(8):1027–34. https://doi.org/10.1177/0022034515587690.

[49] Marsh EJ, Luo H, Wang H. A three-tiered approach to differentiate Listeria monocytogenes biofilm-forming abilities. FEMS Microbiol Lett 2003;228(2):203–10. https://doi.org/10.1016/s0378-1097(03)00752-3.

[50] Takhistov P, George B. Early events and pattern formation in Listeria monocytogenes biofilms. Biofilms 2005;1(4):351–9. https://doi.org/10.1017/S1479050504001504.

[51] Bridier A, Dubois-Brissonnet F, Boubetra A, Thomas V, Briandet R. The biofilm architecture of sixty opportunistic pathogens deciphered using a high throughput CLSM method. J Microbiol Methods 2010;82(1):64–70. https://doi.org/10.1016/j.mimet.2010.04.006.

[52] Serra DO, Richter AM, Klauck G, Mika F, Hengge R. Microanatomy at cellular resolution and spatial order of physiological differentiation in a bacterial biofilm. mBio 2013;4(2). https://doi.org/10.1128/mBio.00103-13. e00103-00113.

[53] Guilbaud M, Piveteau P, Desvaux M, Brisse S, Briandet R. Exploring the diversity of Listeria monocytogenes biofilm architecture by high-throughput confocal laser scanning microscopy and the predominance of the honeycomb-like morphotype. Appl Environ Microbiol 2015;81(5):1813. https://doi.org/10.1128/AEM.03173-14.

[54] Chavant P, Martinie B, Meylheuc T, Bellon-Fontaine M-N, Hebraud M. Listeria monocytogenes LO28: surface physicochemical properties and ability to form biofilms at different temperatures and growth phases. Appl Environ Microbiol 2002;68(2):728. https://doi.org/10.1128/AEM.68.2.728-737.2002.

[55] Mosquera-Fernández M, Rodríguez-López P, Cabo ML, Balsa-Canto E. Numerical spatio-temporal characterization of Listeria monocytogenes biofilms. Int J Food Microbiol 2014;182–183:26–36. https://doi.org/10.1016/j.ijfoodmicro.2014.05.005.

[56] Flemming H-C, Wingender J. The biofilm matrix. Nat Rev Microbiol 2010;8(9):623–33. https://doi.org/10.1038/nrmicro2415.

[57] Lemon KP, Higgins DE, Kolter R. Flagellar motility is critical for *Listeria monocytogenes* biofilm formation. J Bacteriol 2007;189:4418–24. https://doi.org/10.1128/JB.01967-06.

[58] Kearns DB. A field guide to bacterial swarming motility. Nat Rev Microbiol 2010;8(9):634–44. https://doi.org/10.1038/nrmicro2405.

[59] Guttenplan SB, Kearns DB. Regulation of flagellar motility during biofilm formation. FEMS (Fed Eur Microbiol Soc) Microbiol Rev 2013;37(6):849–71. https://doi.org/10.1111/1574-6976.12018.

[60] Nakamura S, Minamino T. Flagella-driven motility of bacteria. Biomolecules 2019;9(7):279. https://doi.org/10.3390/biom9070279.